Concept and performance evaluation of two 3 GHz buncher units optimizing the dose rate of a novel preclinical proton minibeam irradiation facility

Michael Mayerhofer   , Andreas Bergmaier, Gerd Datzmann, Hermann Hagn, Ricardo Helm, Johannes Mitteneder,

Ralf Schubert, Luigi Picardi, Paolo Nenzi, Concetta Ronsivalle, Hans-Friedrich Wirth, Günther Dollinger

Abstract

To demonstrate the large potential of proton minibeam radiotherapy (pMBRT) as a new method to treat tumor diseases, a preclinical proton minibeam radiation facility was designed. It is based on a tandem Van-de-Graaff accelerator providing a 16 MeV proton beam and a 3 GHz linac post-accelerator (designs: AVO-ADAM S.A, Geneva, Switzerland and ENEA, Frascati, Italy). To enhance the transmission of the tandem beam through the post-accelerator by a factor of 3, two drift tube buncher units were designed and constructed: A brazed 5-gap structure (adapted SCDTL tank of the TOP-IMPLART project (ENEA)) and a non-brazed low budget 4-gap structure. Both are made of copper. The performance of the two differently manufactured units was evaluated using a 16 MeV tandem accelerator beam and a Q3D magnetic spectrograph. Both buncher units achieve the required summed voltage amplitude of 42 kV and amplitude stability at a power feed of less than 800 W.

Data Availability: All relevant data are within the manuscript and its Supporting information files.

Competing interests: The authors have declared that no competing interests exist.

Introduction

The number of new cancer cases is increasing worldwide (over 19 million in 2020) [1], at the same time, tumor-induced mortality was be further reduced by 5% on average in Europe between 2015 and 2020 [2]. Radiation therapy contributes to this trend in the majority of all cases and especially charged particle therapy becomes increasingly important [3].

A promising further development in this field is proton minibeam radiotherapy (pMBRT) [4, 5]. Submillimeter planar or pencil-like beams are applied with a beam spacing (centre-to-centre distance (ctc)) much larger than their transverse beam dimensions (at tissue entry). Typical transverse beam dimmensions range from 0.1 mm to about 1 mm and typical ctc values from 0.5 mm to a few millimeters [6, 7]. This results in a transverse dose profile characterized by a pattern of alternating dose maxima (peaks) and dose minima (valleys) and thus a high spatial fractionation of the dose in the normal tissue. A quantity frequently cited in this context is the peak-to-trough dose ratio (PVDR). A high PVDR associated with low valley doses is required to promote maintenance of normal tissue [8]. The biological mechanisms leading to this normal tissue preservation cannot yet be fully explained. However, some relevant mechanisms are summarized in [9, 10]. The lateral spread of protons, caused by small angle scattering, enlarges the individual minibeams with increasing penetration depth toward the target volume. A quasi-homogeneous irradiation and the minimization of the PVDR in the target volume is achieved by the superposition of the individual beams for a combination of transverse beam size and CTS suitable for the specific target depth. The potential of pMBRT has been successfully demonstrated in the past using various biological models as presented for example in [11–16]. First pMBRT treatment plans for treating humans have been simulated which also suggest dosimetric advantages in normal tissues compared to conventional proton therapy [17]. However, mouse ear studies suggest that side effects can be completely avoided only with proton mini-beams that have a transverse dimension of less than σ = 90 µm and a ctc of 1.8 mm at the tissue entrance [13]. Such beam dimensions with a sufficiently high beam current are currently only available to the pMBRT community at the Maier-Leibnitz laboratory in Munich. However, the maximum proton energy and thus the range of the protons is limited there by the terminal voltage of the 14 MV Van-de-Graaff accelerator to 28 MeV (about 6 mm proton range in water) [7]. In order to demonstrate the advantages of pMBRT with transverse beam dimensions σ < 90 µm at higher proton energies and thus for deeper lying tissue, a new concept for a preclinical irradiation facility (shown in Fig 1) was designed and characterised by simulations [18]. A tandem accelerator generates a 16 MeV proton beam of high brilliance that is further accelerated by a 2997.92 MHz linear post accelerator (linac) system to 70 MeV (about 40 mm proton range in water) and focused by a quadrupole triplet on the target. The linac system is based on the commercial system from AVO-ADAM called LIGHT (Linac for Image Guided Hadron Therapy) [19]. It consists of two Side Coupled Drift Tube Linac (SCDTL) structures orignially designed from ENEA for the TOP-IMPLART project [20] and 4 Coupled Cavity Linac (CCL) structures. The advantage using an existing tandem accelerator (like the one situated at the Maier Leibnitz Laboratory in Garching [21]) as injector is the reduced costs compared to the full front-end linac system [19, 20], since the radio-frequency quadrupole (RFQ) and the first modules of the linac can be omitted. Additionally, the tandem accelerator is perfectly suited to generate a bright and high intensity proton beam and can be used for other applications (e.g. materials sciences).
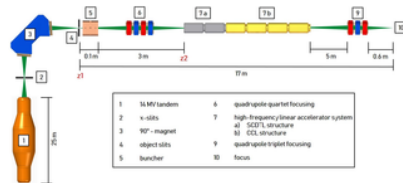
Fig 1. Concept of the preclinical proton minibeam irradiation facility.
A 16 MeV proton beam provided by a tandem is accelerated to 70 MeV by a radio-frequency linac system and subsequently focused to 0.1 x 0.1 mm^2 by a quadrupole triplet. The 6-dimensional phase space of the tandem beam is matched to the accepted phase space of the linac by a buncher unit and a quadrupole quartet.
https://doi.org/10.1371/journal.pone.0258477.g001

To increase the transmission through the post-accelerator, a 2997.92 MHz buncher unit is necessary for adjusting the longitudinal phase space at position z1 coming from the tandem (Fig 2a) with the accepted phase space of the linac (grey dots in Fig 2b). The resulting time focus in front of the linac at position z2 is shown in Fig 2b (colored dots). The RF pulse characteristic of the buncher is adapted to the linac (5 µs at 200 Hz). A quadrupole quartet is used to match the transverse phase space between the tandem and linac.
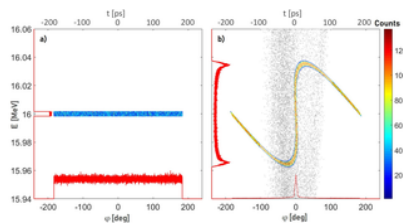

Fig 2. Longitudinal phase space between the tandem and linac.
a) longitudinal phase space at z1 (see Fig 1) coming from the tandem (E_{kin} = 16 MeV, ΔE_{kin} = 0.01%) [18] b) longitudinal phase space in front of the linac at z2 (see Fig 1) (colored dots) and accepted phase space of the linac (grey dots). The red curves along the x- and y-axes are projections of the particle distributions.
https://doi.org/10.1371/journal.pone.0258477.g002

The particle tracking code TRAVEL [22] was used to optimize the buncher peak voltage (buncher amplitude) U_b and the field strength of the quadrupole quartet/triplet to maximize the proton transmission into an area of 0.1 x 0.1 mm^2 at the focus. Fig 3 shows the percentage of protons transmitted from the tandem through the linac into an area of 0.1 x 0.1 mm^2 as a function of U_b. An optimal buncher amplitude of U_b = 42 kV results in a maximum proton transmission of 47%, which is a factor 3 higher than the transmission without a buncher unit [18]. For an average tandem beam current of 40 nA (5 µs at 200 Hz), this results in a beam current of I_B = 19 nA at the focus which is more than sufficient for preclinical experiments. The deposited dose can be changed via the irradiation time and monitored with an ionization chamber. However, the total irradiation time is a crucial parameter for preclinical experiments as well as patient comfort. Therefore, the variation of the buncher amplitude ΔU_b should not lead to a significant change of the dose rate in order to keep the irradiation time as short as possible. Therefore, besides the amplitude U_b, the variance of the amplitude ΔU_b is a key parameter of the buncher.
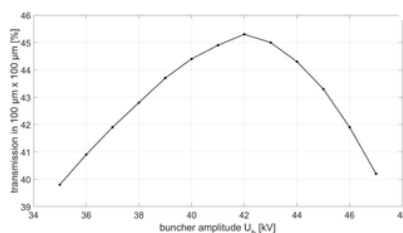
Fig 3. Proton transmission into an area of 0.1 x 0.1 mm^2 at the focus (see Fig 1) as a function of buncher amplitude U_b.
https://doi.org/10.1371/journal.pone.0258477.g003

This paper presents two concepts for a buncher unit which allow an efficient coupling between a tandem pre-accelerator and a linear post-accelerator as required for the described preclinical irradiation facility which offers the perspective to rapidly accelerate pMBRT research. The cavity design of the buncher units is based on the drift tube linac (DTL) concept. The design of both concepts and their performance is presented in the following.

Materials and methods

Buncher unit design

Since there is no commercial solution for the required 3 GHz buncher unit, the buncher concepts presented in the following had to be developed from scratch. Therefore, in addition to the design methods, the following three subsections also describe the RF cavity designs and the frequency tuning systems that comprise the buncher units.

Design methods.

A basic initial design of the cavity geometry is performed in both cases using the SUPERFISH [23] software with the specific code MDTfish. The cavity cells are tuned to a desired resonant frequency by adjusting the drift tube gap length. Then, the key performance indicators of shunt impedance, quality factor and maximum E-field strength are evaluated [24]. Subsequently, a CAD model of the buncher-units with all non-radially symmetric to the beam-axis (z) structures like tuning rods potentially influencing the EM-fields in the cavity is developed and further analyzed using CST-Microwave [25] (hereafter referred to as CST). For the CST simulation, the material property of each component is defined (cavity: high purity copper, etc.). The CST eigenmode solver is used to calculate the electric and magnetic fields of the cavity eigenmodes. Shifts in resonance frequency (f_R) resulting from non-symmetric structures are compensated by iterative fine-tuning of the drift tube gap length.

RF cavity design.

The RF cavity design of both buncher units is based on a drift tube concept as it is already realized for a resonance frequency (f_R) of 2997.92 MHz in linac structures by AVO-ADAM [26] and ENEA [20]. A multi-gap solution was favored to lower the thermal load and to operate the buncher by an existing solid-state amplifier (P_{amp} ≤1350 W). Both cavities are manufactured from OFC copper.

Cavity concept 1 (4-gap) was developed as part of a low-budget and study subject buncher unit. Attached to a CF-100 vacuum pot, it is placed within the beam tube, which makes cost intensive vacuum-tight joining processes (e.g. brazing) unnecessary and mounting of the buncher unit via a CF-100 crosspiece simple. At the same time, the diameter of the CF-100 flange limits the cavity geometry and the number of gaps (see Fig 6). Fig 4 shows cavity concept 1 consisting of 6 individual discs which are pressed together by screws forming 4 individual cells with one gap each. The drift tubes are supported by stems. Pickup loop, excitation loop and copper tuner have access to the cavity through ports.

Fig 4. Cavity concept 1 (4-gap): Three drift tubes are attached by stems.
Pickup loop, excitation loop and copper tuner have access to the cavity through ports. Red line: proton beam.
https://doi.org/10.1371/journal.pone.0258477.g004

Fig 5 shows cavity concept 2 (5-gap) which is adapted from the drift tube part of the Side Coupled Drift Tube Linac (SCDTL) as used in the TOP-IMPLART project [20]. The 5-gap cavity geometry of the TOP-IMPLART SCDTL-2 structure (insertion energy 16.5 MeV) was optimized for 16 MeV (insertion energy SCDTL 2 module of the LIGHT system [27]). The cavity was designed to reach the resonance frequency at a temperature of 42°C. Pickup and excitation loop, variable copper-tuner, and fixed copper tuner have access to the cavity through ports. The drift tube stems contain two cooling channels. All cooling channels are supplied with coolant from a reservoir which is closed by a plate (6a) in which a valve is mounted. After the coolant has passed through the stems, it is collected in a second reservoir (6b) located on the opposite side of the structure. A second valve is mounted at the second reservoir and thus a closed cooling circuit is formed when the chiller system is connected. To enable the operation of the cavity in air and to increase electrical conductivity, the cavity parts were joined by brazing. In addition, the brazing process is necessary to enable the cooling channel system.

Fig 5. Cavity concept 2 (5-gap): Four drift tubes are attached by stems with implemented cooling channels.
Pickup loop, excitation loop, fixed copper tuner and variabe tuner are depicted. Red line: proton beam.
https://doi.org/10.1371/journal.pone.0258477.g005

Table 1 shows the main parameters of the basic cavity designs obtained from SUPERFISH simulations [23]. Taking into account the attenuation due to the required RF equipment, the solid state amplifier provides 950 W to drive the cavities. The input power P_{in} required for a given buncher amplitude U_b can be calculated from the effective shunt impedance Z_{TT} and the overall length L.

$$ \tag{1} $$

Table 1. Parameter list of basic buncher cavities.
https://doi.org/10.1371/journal.pone.0258477.t001

Taking into account a safety margin of 25% for the simulated eff. shunt impedance, an input power of 860 W for the 4-gap concept and respectively 280 W for the 5-gap concept is required to realize U_b = 42 kV. Due to design restrictions of the 4-gap cavity geometry by the CF-100 vacuum pot, the eff. shunt impedance of the 5-gap concept is 2.2 times higher than that of the 4-gap concept. However, both concepts achieve the required performance in SUPERFISH simulations.

Frequency tuning system.

The frequency tuning system (FTS) of both concepts compensate for the expected thermal drift [28] resulting from a change in surrounding temperature or input power and corrects manufacturing inaccuracies. Figs 6 and 7 show the two buncher units, 4-gap and 5-gap, including all ports, loops and tuning components. The 4-gap FTS consists of a variable tuning system (see Fig 6). A copper rod guided by a step motor can be moved in or out of the cavity to tune the cavity to f_R. The 5-gap FTS (see Fig 7) is related to the one of the TOP-IMPLART project [29, 30]. To achieve the resonant frequency f_R, the buncher unit must be operated at a defined temperature of 42°C, which requires the chiller system mentioned earlier. With a suitable chiller system the temperature of the SCDT structures of the TOP-IMPLART linac (consisting of 7 cavities similar to the 5-gap concept) can be kept stable at (42 ± 0.2)°C at an input power of 1.3 MW (5 µs at 200 Hz) [30, 31]. Considering that the maximum P_{in} of the buncher unit is less than 1 permille of the input power of the SCDT structure, it can be assumed that the buncher unit can be supplied by the same chiller system without losing temperature stability. Additionally, a fixed copper tuner can be used to compensate for manufacturing inaccuracies. Fast thermal changes are corrected by a small variable tuning system consisting of a copper rod and a step motor.

Fig 6. 4-gap buncher unit.
Mounted on a CF-100 flange, the cavity can be installed directly in the beam tube. The vacuum pot provides pickup loop, excitation loop and variable tuner access to the cavity.
https://doi.org/10.1371/journal.pone.0258477.g006

Fig 7. 5-gap buncher unit.
Connection to the beam pipe via CF-16 flanges. CF-16 flanges also provide access to the cavity for pickup loop, variable tuner and fixed copper tuner. The excitation loop is mounted on a CF-63 flange.
https://doi.org/10.1371/journal.pone.0258477.g007

Radio frequency system

Fig 8 shows the RF system which is used to operate the buncher units. An RF signal f_R is provided by a signal generator and then amplified up to 1350 W by a solid state amplifier at a duty cycle of 1%. Both are synchronized by means of a gate generator. To minimize the power fluctuations of the amplifier and to protect it from reflected power, a circulator with a 25 W (cw) dummy load is following subsequently. The pickup signal ΔP_{pu} is measured by a power sensor and analyzed with LabVIEW code. To minimize power loss, all components leading to the excitation loop are connected by a cable type with a very low attenuation (14 dB/100 m at 3 GHz). Fig 9 shows the RF signal and (schematically) the gate signal of the signal generator and amplifier in detail for an RF pulse amplified to 900 W. For illustration purposes the time offset between amplified signal and generator signal was corrected. The signal generator provides an 8 µs long RF puls (green), defined by the signal generator gate (dotted line). The amplifier is ramped up (dashed line) with the beginning of the amplifier gate signal (black) and is able to provide full amplification after 5 µs until the gate signal stops. The incoming RF pulse (green) is amplified within this time window of full amplification. The output power is proportional to the amplitude of the RF pulse provided by the signal generator. The power of the amplified RF signal is stable up to 1% for a pulse length of up to 10 µs.

Fig 8. Schematic representation of frequency tuning- and RF system of the two buncher units.
https://doi.org/10.1371/journal.pone.0258477.g008

Fig 9. Signal characteristics of the RF system.
Schematic: gate generator signal and amplifier bias. The time offset between amplified signal and generator signal is corrected for illustration purposes.
https://doi.org/10.1371/journal.pone.0258477.g009

Variable tuner control loop

To keep the resonance frequency f_R stable, both buncher concepts are equipped with a variable tuning rod. Its software control loop is based on the iterative minimization of the standing wave ratio (SWR) as shown schematically in Fig 8. Every second, two power sensors are measuring the forward and reflected power at the dual directional coupler and a LabVIEW-based control algorithm calculates the SWR. When the tuning loop is started, the variable tuner rod is inserted into the cavity until a change in the SWR is detected. Depending on whether the change shows an increase or a decrease compared to the last measured value, the direction of movement of the variable tuner is changed or maintained and is than held until the SWR increases again. This simple low budget control loop can be further optimized by analyzing the phase relationship between the input signal and the pickup signal if the variation of the buncher amplitude needs to be further reduced.

Quality factor measurement

The unloaded quality factor Q_0 (hereafter quality factor) is calculated from the loaded quality factor Q_L. Q_L is, in turn, determined by the 3 dB half-width of the resonance curve of the respective buncher units, which is measured via the pickup loop. The measurements of the resonance curves were performed on the test bench where the SWR (overcoupled) was 1.05 for the 5-gap

concept and 1.15 for the 4-gap concept. The input power was 10 mW (cw) in both cases. The power dissipation caused by the pick-up loop can be neglected, and thus in the case of overcoupling Q_0 results to

$$\tag{2}$$

as shown in [24, 32].

Performance measurement with a 16 MeV proton beam

The performance of the two buncher units is evaluated using a 16 MeV proton beam provided by the Munich tandem Van-de-Graaff accelerator [21] and a Q3D magnetic spectrograph [33, 34] for measuring the energy spectrum of the protons behind the buncher. The measurement setup is shown in Fig 10. During the measurements, the buncher unit under test, situated directly upstream of the Q3D, is operated with the variable tuner control loop and radio frequency system (8 µs at 200 Hz). The electric potential U oscillating in the cavity gaps with the resonance frequency f_R modulate the kinetic energy E_{kin} of the protons sinusoidally as they traverse the buncher. Depending on the buncher amplitude, this results in a characteristic energy redistribution of the protons in the longitudinal phase space (see Fig 2). The existing Q3D setup offers the possibility to measure the resulting energy histograms. Comparable to a 270° analysis magnet in combination with a segmented focal plane detector, the deflection radius of particles can be determined in relation to their energy. The detector offers a spatial resolution of 1 mm and the maximum deflection of approx. 1 m in the focal plane caused by the magnet corresponds to an energy variation of 10%. Therefore, in the case of the 16 MeV protons, the Q3D offers an excellent energy resolution of up to and at the same time the possibility to measure the entire energy histogram at once. To protect the focal plane detector from overstressing, the beam is reduced to ≈ 300 by a chopper unit (7 µs at 200 Hz) and microslits. A gate generator is used to synchronize the chopper system and the RF system of the buncher unit so that the proton bunches reach the buncher unit 100 ns after the start of the excitation of the cavtiy by the RF pulse (see Fig 9).

Fig 10. Measurement setup for performance evaluation using a tandem accelerator and a Q3D magnetic spectrograph.
https://doi.org/10.1371/journal.pone.0258477.g010

Buncher amplitude stability measurement

The measurements to evaluate the stability of the buncher amplitude are carried out on the test bench in the RF-laboratory at a pressure of 10^{-7} mbar. The variable tuner control loop and the RF system, together with the buncher units described below, represent the test setup for these measurements. Using a dummy load, the signal generator and amplifier are brought to operating temperature before the measurements. Thus only the thermal drift caused by the input power applied to the cavity and changes in surrounding temperature need to be compensated by the control loop of the frequency tuning system. The pick-up signal P_{pu} is proportional to the buncher amplitude . Thus, the variation of the pick-up signal ΔP_{pu} caused by the frequency tuning process is a measure for the stability of the buncher.

Results and discussion

Radio frequency system evaluation

Fig 11 shows a 32 hour long-term output signal measurement of the RF system (input signal of the buncher units) performed to estimate the stability of the RF system. The entire attenuation of the signal between amplifier output and excitation loop amounts to approx. 1.1 dB, so that 1050 W are available. The buncher unit is replaced by an RF attenuator (40 dB, 200 W) for the measurement (see Fig 8) and the output of the attenuator is connected with a power sensor (same model as in Fig 8). Each measured value of the long-term measurement results from the average of 100 single measurements taken in a measuring interval of 6 µs starting 1 µs after the RF pulse (see Fig 9). The 95% coefficient limits for the maximum and minimum input power signal are calculated from the relative measurement uncertainties specified in the sensor manual of 0.05 dB (at 3 GHz) [35]. Maximum and minimum input powers deviate from the mean input power by about ±1.5%, representing the accuracy with which the absolute value of P_{in} can be set. However, during irradiation, the input power is adjusted to achieve a maximum beam current, thus only the variation of the input power affects the variation of the beam current. In case of the 4-gap concept the maximum input power variation of about ±0.4% (at P_{in} = 795 W) results in a variation of the buncher amplitude of ΔU_b = ±0.1kV. The TRAVEL simulation of the presented preclinical proton minibeam irradiation facility shown in [18] were performed for the corresponding buncher amplitude U_b of 41.9 kV and 42.1 kV. This results in a variation of the maximum beam current of the irradiation facility (19 nA) of ±0.08%, which does not limit the planned preclinical experiments.

Fig 11. Input power stability measurement.
Measuring time: 32 h.
https://doi.org/10.1371/journal.pone.0258477.g011

Quality factor evaluation

All non-radially symmetric structures in the cavity and the change of the cavity geometry due to the movement of the variable tuner influence the electromagnetic field and consequently results in a change of the eff. shunt impedance Z_{TT}. The unloaded quality factor Q_0 of a cavity is proportional to its shunt impedance and therefore is a performance benchmark. Q_0 was determined as described in the section Quality factor measurement and simulated with CST for both concepts for various tuner positions to evaluate the change in Z_{TT} (Table 1) calculated by SUPERFISH. For both concepts, the lowest unloaded quality factor is measured with the tuning rod extended to its maximum, i.e. the tuning rod inserted deepest into the cavity. Table 2 shows the unloaded quality factor Q_0 for the expected (exp.) tuner position (arcording to the CST simulation) to reach the resonance frequency f_R with the required input power and for the maximum (max.) extended tuning rod.

Table 2. Simulated and measured unloaded quality factor Q_0 for the expected (exp.) tuner position to reach f_R and for the maximum (max.) extended tuning rod of both buncher units.
https://doi.org/10.1371/journal.pone.0258477.t002

The measured unloaded quality factor of the 4-gap concept for the tuner position to reach f_R is 6% smaller than the simulated one. This was expected since un-brazed cavities were reported to have a 7%—9% lower Q_0 compared to brazed ones [36]. Besides, the surface conductivity may be reduced due to surface imperfections from machining. The measured unloaded quality factor of the 5-gap concept for the tuner position to reach f_R is reduced by about 1% compared to the simulated Q_0. The unloaded quality factor of the 5-gap concept for the expected tuner position simulated with CST is about 19% reduced to the one simulated with SUPERFISH (Table 1). This is mainly due to the non-symmetric stems of the 5-gap concept (caused by the internal cooling channels), which cannot be included in the SUPERFISH simulation. The measured and simulated unloaded quality factor and therefore the eff. shunt impedance of both concepts correspond to the values calculated with SUPERFISH within the safety performance margin of 25% for both tuner positions. The buncher amplitude U_b required for the preclinical irradiation facility is achieved for both concepts in the entire tuner range.

Performance measurement

The performance of the buncher units is evaluated using a 16 MeV proton beam provided by a tandem accelerator and a Q3D magnetic spectrograph. Fig 12 shows an example of an energy histogram (4-gap concept, P_{in} = 778 W) where the x-axis represents the proton energy E_{kin} (channel 0: E_{kin} = 16 MeV). The energy resolution given by the energy spread of the tandem together with the resolution of the Q3D setup was measured as a Gaussian $f(U|\sigma)$ of σ = 1.7 keV (). The energy distribution function of a sinusoidal RF modulated beam without energy spread is derived in S1 Appendix for a maximum effective integrated buncher amplitude U_b. It is transformed into a particle distribution function $g(U|U_b)$

$$ \tag{3} $$

that gives the number of detected particles N in dependence of the acceleration voltage U (see also S1 Appendix). The constant C is proportional to the total number of measured particles. The convolution of the energy resolution with the characteristic sinusoidally modulated distribution function results in the fit function

$$ \tag{4} $$

that is added to the measured data (red line in Fig 12). Thus, the buncher amplitude U_B can be determined resulting in (42.98 ± 0.24) kV for the energy histogram shown in Fig 12. The distance between the two maxima in the Q3D focal plane is about 5.4 cm.

Fig 12. Energy distribution of the bunched protons recorded with the Q3D magnetic spectrograph setup (P_{in} = 778 W, 4-gap buncher).
https://doi.org/10.1371/journal.pone.0258477.g012

Fig 13 shows the evaluated amplitudes U_b as a function of P_{in} for both buncher units. The measurements (black: 4-gap concept, pink: 5-gap concept) are fitted with the function $y(x) = (a \cdot x)^{1/2}$ where a represents $Z_{TT} \cdot L$ (compare Eq 1). The dashed curves are the confidence limits (95%) for these fits. The measurement error ΔU_b was calculated using the χ^2-squared-method to evaluate the quality of the fit. The red and green curves show the simulated performance for both concepts as calculated from the eff. shunt impedance simulated in SUPERFISH (see Table 1) using Eq 1. The performances due to the measured unloaded quality factor (see Table 2) is shown in light blue and dark blue. The performance measured on the Q3D setup correspond largely to the reduced eff. shunt impedance (resulting from the measured Q_0) in both cases. The differences between simulated optimum and the measurement corresponds to the reduction of the cavity unloaded quality factor Q_0 as discussed in section quality factor evaluation. The fit functions and the confidence intervals result in Z_{TT} = 32.25 ± 0.40 for the 4-gap concept and Z_{TT} = 55.49 ± 6.9 for the 5-gap concept. The required buncher amplitude U_b = 42 kV is achieved for an input power of 751 W for the 4-gap cavity and of 349 W for the 5-gap cavity. Compared to the simulated Z_{TT} values (see Table 1), the measured Z_{TT} values are reduced by about 8% for the 4-gap concept and 28% for the 5-gap concept. This was expected since the quality factors of the two concepts were similarly reduced compared to the SUPERFISH simulation. The reduction of the Z_{TT} values is again due to the fact that the individual parts of the 4-gap concept were not connected by soldering respectively due to the large non-radially symmetrical stems of the 5-gap concept.

Fig 13. Performance of the two buncher concepts.
Black and pink: Measurement series of the accelerator voltage U_b as a function of the input power P_{in}, performed on the Q3D. Green and Red: "Best Case" scenario simulations. Light blue and dark blue: reduced measured quality Q_0.
https://doi.org/10.1371/journal.pone.0258477.g013

Buncher amplitude stability measurement

Fig 14 shows a six-hour buncher amplitude stability measurement of the 4-gap concept at an input power of 800 W (8 µs at 200 Hz). Each value represents the average of 100 single pickup signal measurements over a measurement window of 6 µs starting 1 µs after the RF pulse as described in Fig 9. The 95% coefficient interval for the maximum and minimum pick-up signal is calculated from the relative uncertainty for power measurements of 0.05 dB (at 3 GHz) [35]. This represents the accuracy with which the absolute value of U_b can be set. However, during irradiation, the input power is adjusted to achieve a maximum beam current, thus only the variation of U_b affects the variation of the beam current. The pick-up signal shows a variation of $\Delta P_{pu} = \pm 1.5\%$ during this time and therefore a variation of the buncher amplitude of $\Delta U_b = \pm 0.31$kV is expected. In the case of the preclinical irradiation facility, this corresponds to a variation of the proton transmission in 0.1 x 0.1 mm^2 (as can be seen in Fig 3) and thus a maximum variation of the beam current of less than $\pm 0.3\%$. The variation of the buncher amplitude therefore has no significant effect on the dose rate. A large deviation to lower dose rates would prolong the application time of each spot and in consequence the whole treatment time. Additionally, low dose rates can lead to problems of the dose detection accuracy. Clinically used dose-monitoring systems accept typically a dose rate variation of a factor of two or more in both directions [37].

Fig 14. Pick-up signal measurement of the 4-gap concept with 800W (8 µs at 200 Hz) input power.
Black line: Mean of the pick-up signal, red line: maximum pick-up signal and blue line minimum pick-up signal. Dashed lines: 95% coefficient interval of maximum and minimum pick-up signal.
https://doi.org/10.1371/journal.pone.0258477.g014

As already described in section RF cavity design, the temperature of the 5-gap concept is stabilized by a chiller system. This system is not yet available for long-term measurements, as it is part of the future linac system. The stability of the 5-gap concept is therefore based on the assumption that the system can be operated at $(42 \pm 0.2)°$C. The shift in f_R due to this expected temperature drift results in . For the tuning rod positions at which this frequency shift is compensated (relative to the expected tuning stab position), a variation of the unloaded quality factor and thus the eff. shunt impedance of was measured. The Q_0 values associated with these tuning rod positions were measured as described in section Materials and methods with 10 mW cw input power. Using Eq 1 and taking into account the measured stability of the RF system of (see Fig 11), this results in a maximum change (95% confidence interval) of the buncher amplitude of about ± 0.12kV and thus a beam current stability of $\approx \pm 0.1\%$. The standing wave ratio (SWR) at the excitation loop and the quality of the vacuum show no significant changes which would indicate multipactor effects or sparking during all the test measurements (and Q3D measurements). Therefore, both buncher units can be operated long-term without loss of performance at the tested input powers. Both buncher units therefore outperform the stability requirements for a preclinical irradiation facility.

Conclusion

Two 2997.92 MHz buncher units were developed and manufactured. The measured performance meets the expectations and the required buncher amplitude of 42 kV to provide the maximum beam current for preclinical experiments is achieved in both cases. The stability of the buncher amplitude ΔU_b and the resulting beam current variation of less than 0.3% in case of the 4-gap concept is more than sufficient for preclinical experiments and can be assumed to be even more stable for the temperature stabilized 5-gap concept. Therefore, both concepts outperform the requirements for the planned preclinical minibeam irradiation facility. In general, it was shown that the presented simple buncher concept, even as a low-budget version, offers a performance with which in previous simulations the beam current of a tandem pre-accelerator and linear post-accelerator combination could be increased by a factor of 3 [18]. Thus, the central, non-commercially available component of the planned preclinical proton minibeam irradiation system has been successfully developed and its performance evaluated.

Supporting information

S1 Appendix. Energy distribution function.
https://doi.org/10.1371/journal.pone.0258477.s001
(PDF)

References

1. Sung H, Ferlay J, Siegel RL, Laversanne M, Soerjomataram I, Jemal A, et al. Global cancer statistics 2020: GLOBOCAN estimates of incidence and mortality worldwide for 36 cancers in 185 countries. CA: a cancer journal for clinicians. 2021;71(3):209–249.
View Article • Google Scholar

2. Carioli G, Bertuccio P, Boffetta P, Levi F, La Vecchia C, Negri E, et al. European cancer mortality predictions for the year 2020 with a focus on prostate cancer. Annals of Oncology. 2020;31(5):650–658. pmid:32321669
View Article • PubMed/NCBI • Google Scholar

3. Yuan TZ, Zhan ZJ, Qian CN. New frontiers in proton therapy: applications in cancers. Cancer Communications. 2019;39(1):1–7. pmid:31640788
View Article • PubMed/NCBI • Google Scholar

4. Zlobinskaya O, Girst S, Greubel C, Hable V, Siebenwirth C, Walsh DW, et al. Reduced side effects by proton microchannel radiotherapy: study in a human skin model. Radiation and environmental biophysics. 2013;52(1):123–133. pmid:23271171
View Article • PubMed/NCBI • Google Scholar

5. Prezado Y, Fois GR. Proton-minibeam radiation therapy: A proof of concept. Medical physics. 2013;40(3):031712. pmid:23464307
View Article • PubMed/NCBI • Google Scholar

6. Meyer J, Eley J, Schmid TE, Combs SE, Dendale R, Prezado Y. Spatially fractionated proton minibeams. The British journal of radiology. 2019;92(1095):20180466. pmid:30359081
View Article • PubMed/NCBI • Google Scholar

7. Datzmann G, Sammer M, Girst S, Mayerhofer M, Dollinger G, Reindl J. Preclinical challenges in proton minibeam radiotherapy: physics and biomedical aspects. Frontiers in Physics. 2020;8:471.
View Article • Google Scholar

8. Dilmanian FA, Button TM, Le Duc G, Zhong N, Peña LA, Smith JA, et al. Response of rat intracranial 9L gliosarcoma to microbeam radiation therapy. Neuro-oncology. 2002;4(1):26–38. pmid:11772430
View Article • PubMed/NCBI • Google Scholar

9. Reindl J, Girst S. pMB FLASH-Status and Perspectives of Combining Proton Minibeam with FLASH Radiotherapy. Journal of Cancer Immunology. 2019;1(1).
View Article • Google Scholar

10. Guardiola C, Peucelle C, Prezado Y. Optimization of the mechanical collimation for minibeam generation in proton minibeam radiation therapy. Medical physics. 2017;44(4):1470–1478. pmid:28129665
View Article • PubMed/NCBI • Google Scholar

11. Girst S, Greubel C, Reindl J, Siebenwirth C, Zlobinskaya O, Walsh DW, et al. Proton minibeam radiation therapy reduces side effects in an in vivo mouse ear model. International Journal of Radiation Oncology* Biology* Physics. 2016;95(1):234–241.
View Article • Google Scholar

12. Prezado Y, Jouvion G, Hardy D, Patriarca A, Nauraye C, Bergs J, et al. Proton minibeam radiation therapy spares normal rat brain: Long-Term Clinical, Radiological and Histopathological Analysis. Scientific reports. 2017;7(1):1–7. pmid:29089533
View Article • PubMed/NCBI • Google Scholar

13. Sammer M, Zahnbrecher E, Dobiasch S, Girst S, Greubel C, Ilicic K, et al. Proton pencil minibeam irradiation of an in-vivo mouse ear model spares healthy tissue dependent on beam size. PloS one. 2019;14(11). pmid:31765436
View Article • PubMed/NCBI • Google Scholar

14. Sammer M, Teiluf K, Girst S, Greubel C, Reindl J, Ilicic K, et al. Beam size limit for pencil minibeam radiotherapy determined from side effects in an in-vivo mouse ear model. PloS one. 2019;14(9).
View Article • Google Scholar

15. Prezado Y, Jouvion G, Guardiola C, Gonzalez W, Juchaux M, Bergs J, et al. Tumor control in RG2 glioma-bearing rats: a comparison between proton minibeam therapy and standard proton therapy. International Journal of Radiation Oncology* Biology* Physics. 2019;104(2):266–271. pmid:30703513
View Article • PubMed/NCBI • Google Scholar

16. Lamirault C, Doyère V, Juchaux M, Pouzoulet F, Labiod D, Dendale R, et al. Short and long-term evaluation of the impact of proton minibeam radiation therapy on motor, emotional and cognitive functions. Scientific reports. 2020;10(1):1–14.
View Article • Google Scholar

17. Lansonneur P, Mammar H, Nauraye C, Patriarca A, Hierso E, Dendale R, et al. First proton minibeam radiation therapy treatment plan evaluation. Scientific reports. 2020;10(1):1–8. pmid:32341427
View Article • PubMed/NCBI • Google Scholar

18. Mayerhofer M, Datzmann G, Degiovanni A, Dimov V, Dollinger G. Magnetically focused 70 MeV proton minibeams for preclinical experiments combining a tandem accelerator and a 3 GHz linear post-accelerator. Medical Physics. 2020.
View Article • Google Scholar

19. Degiovanni A, Adam J, Aguilera Murciano D, Ballestrero S, Benot-Morell A, Bonomi R, et al. Status of the Commissioning of the LIGHT Prototype. In: 9th Int. Particle Accelerator Conf.(IPAC'18), Vancouver, BC, Canada, April 29-May 4, 2018. JACOW Publishing, Geneva, Switzerland; 2018. p. 425–428. Available from: https://cds.cern.ch/record/2665490.

20. Ronsivalle C, Carpanese M, Marino C, Messina G, Picardi L, Sandri S, et al. The Top-Implart Project. The European Physical Journal Plus. 2011;126(7):68.
View Article • Google Scholar

21. Dollinger G, Faestermann T. Physics at the Munich Tandem Accelerator Laboratory. Nuclear Physics News. 2018;28(1):5–12.
View Article • Google Scholar

22. Perrin A, Amand J, Mütze T. Travel v4. 06, user manual. CERN internal note. 2003.

23. Halbach K, Holsinger RF. SUPERFISH—a computer program for evaluation of cavities with cylindrical symmetry. Part Accel. 1976;7:213–222. Available from: http://cds.cern.ch/record/700607/files/p213.pdf.
View Article • Google Scholar

24. Wangler TP. RF Linear accelerators. John Wiley & Sons; 2008.

25. Dassault Systèmes Simulia Corp (France). Software: CST STUDIO SUITE. Version 2021.03. Web page: https://www.3ds.com/de/produkte-und-services/simulia/produkte/cst-studio-suite/.

26. Ungaro D, Stabile P, Degiovanni A. LIGHT: A Linear Accelerator for Proton Therapy; 2017.

27. Degiovanni A, Stabile P, Ungaro D, SA A. LIGHT: a linear accelerator for proton therapy. Proceedings of NAPAC2016, Chicago, USA. 2016.

28. Ciambrella M, Cardelli F, Migliorati M, Mostacci A, Palumbo L, Ficcadenti L, et al. ELECTROMECHANICAL ANALYSIS OF SCDTL STRUCTURES. 2014.

29. Surrenti V, Nenzi P, Ronsivalle C, Ambrosini F, Picardi L, Bazzano G. RF system design for the TOP-IMPLART accelerator. 2015.

30. Nenzi P, Ampollini A, Bazzano G, Marracino F, Picardi L, Ronsivalle C, et al. Status of the TOP-IMPLART Proton LINAC. TUPWI004, these proceedings, IPAC '015, Richmond (VA), USA. 2015.

31. Ronsivalle C, Picardi L. Electromechanical analysis of scdtl structures. In: 5th International Particle Accelerator Conference, IPAC 2014. Joint Accelerator Conferences Website (JACoW); 2014.

32. Joshi MK, Vyas SK, Tiwari T, Bhattacharjee R. Design of coaxial cavity for high power magnetron. In: 2017 Conference on Microwave Techniques (COMITE). IEEE; 2017. p. 1–5.

33. Neumaier P, Dollinger G, Bergmaier A, Genchev I, Görgens L, Fischer R, et al. High-resolution elastic recoil detection utilizing Bayesian probability theory. Nuclear Instruments and Methods in Physics Research Section B: Beam Interactions with Materials and Atoms. 2001;183(1-2):48–61.
    View Article • Google Scholar

34. Wirth H, Angerer H, von Egidy T, Eisermann Y, Graw G, Hertenberger R. New Q3D focal plane detector with cathode-strip readout became operational. Maier-Leibnitz-Laboratorium; 2000. p. 71. Available from: https://www-old.mll-muenchen.de/bl_rep/jb2000/p71.ps.

35. Rohde; Schwarz GmbH. Rohde and Schwarz NRP Power Meter Family Specifications. 2018;06.00.

36. Marcellini F, Keil B, Rohrer M, Stadler M, Stettler J, Treyer DM, et al. Design of cavity BPM pickups for Swissfel. Proc IBIC. 2012;12.

37. Gillin MT, Sahoo N, Bues M, Ciangaru G, Sawakuchi G, Poenisch F, et al. Commissioning of the discrete spot scanning proton beam delivery system at the University of Texas MD Anderson Cancer Center, Proton Therapy Center, Houston. Medical physics. 2010;37(1):154–163. pmid:20175477
    View Article • PubMed/NCBI • Google Scholar